

**DANISH METEOROLOGICAL INSTITUTE**

---

**SCIENTIFIC REPORT**

---

**03-20**

**Radio Occultation retrieval  
of Atmospheric Absorption  
based on FSI**

**Martin S. Lohmann, Arne Skov Jensen,  
Hans-Henrik Benzon, Alan Steen Nielsen**



**COPENHAGEN 2003**



**ISSN-Nr. 1399-1949 (Online)**  
**ISBN-Nr. 87-7478-521-4**

---

## List of Contents

1	Introduction	5
2	Retrieval of Complex Refractivity	7
3	Application of FSI in a LEO-LEO Link	10
4	Analysis of Gibb's Phenomenon	12
5	Windowed FSI	17
6	Noise Impact	21
7	Windowed FSI of Simulated RO Signals	24
8	Summary and Conclusion	30
9	References	32

---

## Abstract

In this report it is shown how the Full Spectrum Inversion (FSI) technique can be applied in connection with LEO-LEO absorption measurements. In order to derive atmospheric water vapour profiles from LEO-LEO radio occultations, it is essential to correctly retrieve the complex refractivity index from measured signal attenuations and Doppler shifts. Complex refractivity profiles are readily computed from profiles of bending angles and signal attenuations, measured as functions of ray impact parameters, through Abelian transforms.

When the FSI technique is applied to a radio occultation signal both bending angle and signal attenuation are automatically assigned to the corresponding impact parameter. This property makes the FSI technique very suitable for inversion of LEO-LEO cross-link measurements.

However, as the observed time series are always finite the computed Fourier Spectrum, which is an integral part of the FSI technique, will suffer from artificial oscillations caused by Gibb's phenomenon if this Fourier integral is evaluated following standard formulas. For typical atmospheric conditions these oscillations are in the same order of magnitude as the amplitude variations induced by the Earth's atmosphere. Consequently, the FSI based absorption measurements will be very noisy if these artificial oscillations are not removed. In this report it is demonstrated how Gibb's phenomenon can be significantly reduced if window functions of varying durations are applied to the FSI Fourier integral. It is also shown that the windowed FSI (WFSI) is less sensitive to noise than the standard FSI. We will derive the window approach for the FSI technique, which is anticipated to work also for other methods based on a Fourier operator e.g. the canonical transform (CT).

Application of the WFSI is demonstrated by applying this technique to a 10 GHz signal in a LEO-LEO cross link. The signal is generated by solving Helmholtz equation for a complex refractivity index field. Excellent agreement is found between computed bending angle and attenuation profiles and the original true input profiles for single path propagation. In multipath regions only the bending is retrieved correctly whereas the retrieved attenuation is strongly biased as compared to the true profiles in the part of the multipath region where the fastest phase variations occur. The simulations also reveal that the WFSI technique is less sensitive to white noise and ringing than the FSI technique.

Though the WFSI technique has been derived in order to accurately determine the amplitude of the transformed field in a LEO-LEO link it may also be useful for traditional processing of GNSS-LEO radio occultation signals as it is less sensitive to additive noise, Gibb's phenomenon, and tracking errors compared to the standard FSI. However, the WFSI requires somewhat more CPU power than the standard FSI.

---

# 1 Introduction

Temperature, pressure, and humidity profiles of the Earth's atmosphere can be derived through the radio occultation technique. This technique is based on the Doppler shift imposed, by the atmosphere, on a signal emitted from a GPS satellite and received by a Low Earth Orbiting (LEO) satellite, see e.g. [Rocken *et al.*, 1997 Kursinski *et al.* 1997 and Kursinski *et al.*, 2000]. The method is very accurate with a temperature accuracy of one degree Kelvin, when both frequencies in the GPS system are used.

However, when using GPS frequencies, retrieval of atmospheric water vapour requires a priori information of the atmospheric state to separate the contribution from water vapour and temperature. In order to avoid use of external data more sophisticated satellite systems have been proposed where the atmosphere is sounded through additional LEO-LEO cross-links [Kursinski *et al.*, 2002; Eriksson *et al.*, 2003]. The carrier frequencies used in these LEO-LEO links must be located around a water vapour absorption line to enable detection of both phase and amplitude modulations caused by the atmosphere. For instance, the ESA ACE+ Earth Explorer Opportunity mission proposes to use additional LEO-LEO links with three frequencies around the 23 GHz water vapour line; namely 10, 17, and 23 GHz [Høeg and Kirchengast, 2002]. The principle of combined LEO-LEO and GPS-LEO cross-links is illustrated in Figure 1.

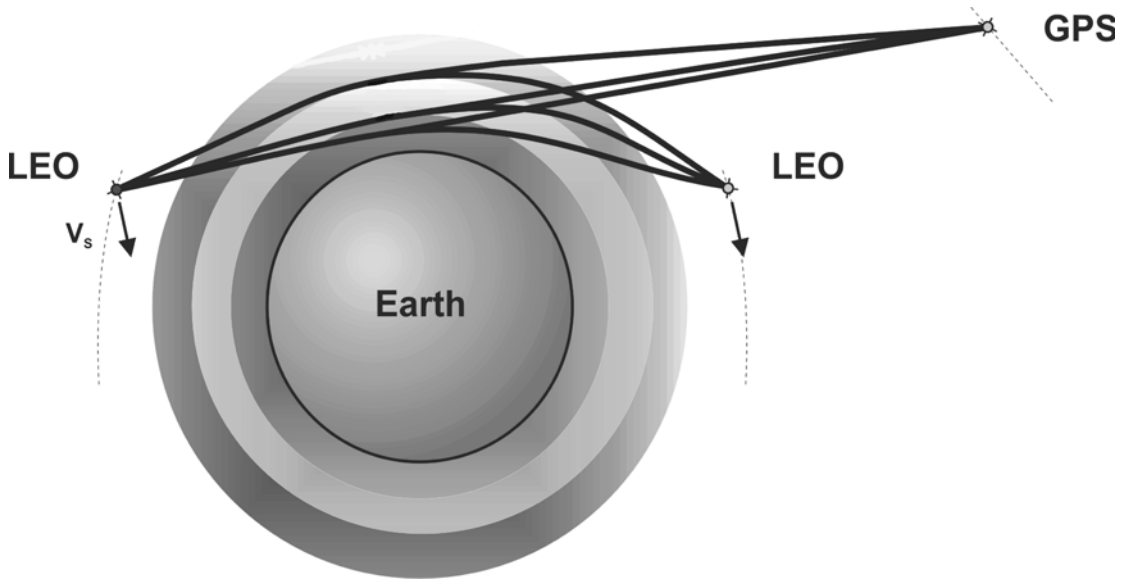


**Figure 1-1:** Principle of combined LEO-LEO and GPS-LEO cross-links. Radio waves emitted by either a LEO or a GPS satellite are received by a LEO satellite setting behind the Earth's limb providing a vertical scan of the atmosphere. The LEO-LEO-links are sensitive to both ray bending and atmospheric absorption allowing independent observations of water vapor.

In order to derive independent profiles of atmospheric water vapour from radio occultations at frequencies around a water vapour absorption line, it is essential, for each frequency, to correctly retrieve the complex refraction index [Leroy, 2001a and

---

*Lohmann et al.* 2003]. Under the assumption of spherical symmetry, a complex refractivity profile is readily computed, through Abelian transforms, from a profile of bending angle and a profile of optical depth measured as functions of ray impact parameter [*Leroy*, 2001a and *Nielsen et al.* 2003].

Alternatively, geophysical parameters can also be derived from observations of the variations in the absorption coefficient with frequency by using pairs of frequencies (calibrations frequencies/tones) [*Kursinski et al.* 2002 and *Nielsen et al.* 2003]. In this approach geophysical parameters are derived from a profile of real refractivity plus measured variations in imaginary refractivity as function of frequency. These variations are computed by an Abel transform, assuming spherical symmetry, of a profile representing the differences between two absorption profiles computed at two different frequencies. In this report we focus on retrieval of imaginary refractivity profiles, i.e., we do not consider calibration tones, though it should be noted that the techniques described here are equally applicable for observations with calibration frequencies.

For a given frequency a profile of transmission as a function of ray impact parameter can be derived using either geometrical optics or radio holographic methods. [*Leroy*, 2001] describes how transmission profiles can be computed using geometrical optics whereas [*Gorbunov*, 2002a] suggests the use of the canonical amplitude in order to establish the transmission profile. The major advantage of radio holographic methods as compared to geometrical optics is that the former methods can disentangle multipath [*Nielsen et al.* 2003]. So far, six high resolution methods have been proposed for processing of radio occultation signals in multipath regions: (1) back-propagation [*Gorbunov et al.*, 1996; *Hinson et al.*, 1997, 1998; *Gorbunov and Gurvich*, 1998], (2) radio-optics, [*Lindal et al.*, 1987; *Pavelyev*, 1998; *Hocke et al.*, 1999; *Sokolovskiy*, 2001; *Gorbunov*, 2001], (3) Fresnel diffraction Theory [*Marouf et al.*, 1986; *Mortensen and Høeg*, 1998; *Meincke*, 1999], (4) canonical transform [*Gorbunov*, 2002a, *Gorbunov* 2002b], (5) full spectrum inversion (FSI) [*Jensen et al.*, 2003a; *Gorbunov et al.*, 2003], and (6) phase matching [*Jensen et al.*, 2003b].

In terms of resolution and ability to handle multipath, the most efficient radio holographic methods are currently the Fourier operator based methods; canonical transform, FSI, and phase matching. However, when Fourier operator based methods are used to compute transmission profiles the resulting profiles will suffer from artificial oscillations caused by Gibb's phenomenon [*Proakis and Manolakis*, 1996] due to the finite duration of the measured signal. A similar problem is encountered when the back-propagation method is used as discussed by [*Leroy*, 2001b].

Below, we will demonstrate how window functions with varying length can be used to significantly reduce oscillations caused by Gibb's phenomenon when the FSI technique is applied to RO signals. Furthermore, it is also shown that for RO signals the windowed Fourier transform is less sensitive to noise than the global Fourier transform. Though this report focus on the application of the FSI technique it should be noted that the window approach described here can be applied also to other radio holographic methods.

The first attempt to use window functions with Fourier Operator based methods was proposed by [*Beyerle et al.*, 2003] who introduced a heuristic method combining the canonical transform and the radio optic techniques. The aim of this method is to reduce negative refractivity bias introduced by tracking error using a square window with constant length. The method which will be presented in this report is different; it is based on smooth window functions of varying length applied in order to reduce ringing in the transformed field. However, the findings by [*Beyerle et al.*, 2003] that

window functions can reduced the impact of tracking errors are also expected to be applicable to the technique presented in this study.

The report is organized in the following structure: Section 2 describes the principles of deriving complex refractivity. In Section 3 we briefly review the FSI method and discuss advantages and disadvantages of this technique in relation to absorption measurements. Section 4 presents an analysis of the of Gibb's phenomenon in RO signals. In Section 5 the windowed FSI technique is described. Section 6 presents an analysis of the impact of white noise. Results from numerical simulations are presented in Section 7 where we apply the WFSI to simulated signals with both absorption and multipath.

## 2 Retrieval of Complex Refractivity

Radio waves transverse the Earth's atmosphere from a LEO or GPS satellite to a receiving LEO satellite are subject to diffraction, refraction, and absorption. For frequencies in the L- and X/K-band the importance of these phenomena depend upon the complex refraction index field being a function of the temperature distribution, pressure, water vapour, liquid water, frequency and the electromagnetic field [*Liebe, 1989*]. When diffraction effects are small relative to the effects of absorption the measured signal can be interpreted using geometrical optics (GO). This is generally the case for Earth atmospheric RO observations at GPS or higher frequencies, excluding regions with strong focusing where diffraction effect may become significant as demonstrated by [*Kursinski et al., 1997; Kursinski et al., 2002*].

When the GO approximation (small wavelength) is valid the ray trajectory through the atmosphere are determined by the real part of the complex refraction index field,  $n'$ , whereas the imaginary part of the refraction index,  $n''$  determines the absorption along these ray paths. Using GO approximation, the incremental variation in the position vector,  $\mathbf{r}$ , along a ray trajectory,  $s$ , and the incremental amplitude attenuation,  $dA/ds$  may be expressed as [*Born and Wolf, 1999*]:

$$\frac{d}{ds} \left( n' \frac{d\mathbf{r}}{ds} \right) = \nabla n'(\mathbf{r}) \quad (2-1)$$

and

$$\frac{dA}{ds} = -2kn''(\mathbf{r})A ds \quad (2-2)$$

The total bending,  $\alpha$ , and the total absorption for a given ray may be computed by integrating the incremental bending and the incremental absorption along the ray path determined by (2-1). In a spherically symmetric atmosphere the total ray bending,  $\alpha$ ,

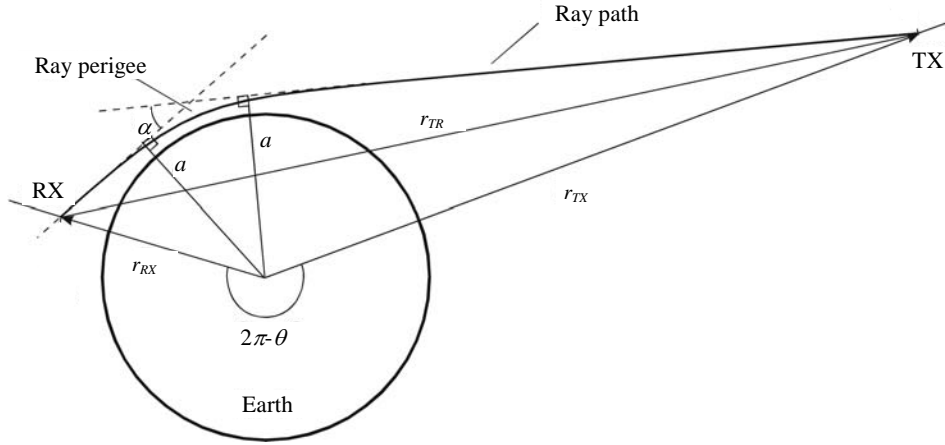


**Figure 2-1:** Geometry of radio occultation. The radio waves propagate from a transmitter, TX, to a receiver, RX, through the Earth's atmosphere.

and absorption can readily be computed using the following Abelian transforms [Leroy, 2001a and Kursinski et al., 2002], see also definition sketch in Figure 2-1.

$$\alpha = -2 \int_{r_i}^{\infty} \frac{a}{\sqrt{(n'(r)r)^2 - a^2}} \frac{d \ln(n'(r))}{dr} dr \quad (2-3)$$

$$\ln \left( \frac{A_{RX}}{A_{TX}} \right) = -2k \int_{r_i}^{\infty} \frac{n''(r)n'(r)r}{\sqrt{(n'(r)r)^2 - a^2}} dr \quad (2-4)$$

where  $r$  is distance from the ray trajectory to the centre of curvature,  $r_i$  is the smallest value of  $r$ , and  $A_{RX}$  and  $A_{TX}$  are the ray amplitude at the receiver and transmitter, respectively. The Abelian inverse of (2-3) and (2-4) are [Leroy, 2001a, Kursinski et al., 2002, Nielsen et al., 2003]:

$$\ln(n'(a_t)) = -\frac{1}{\pi} \int_{a_t}^{\infty} \frac{\alpha(a)}{a_t \sqrt{a^2 - a_t^2}} da, \quad r_i = \frac{a_t}{n'(a_t)}, \quad (2-5)$$

and

$$n''(a_t) = \frac{1}{\pi k} \frac{da}{dr} \Big|_{a=a_t} \int_{a_t}^{\infty} \frac{d \ln \left( \frac{A_{RX}}{A_{TX}} \right)}{da} \frac{1}{\sqrt{a^2 - a_t^2}} da, \quad r_i = \frac{a_t}{n'(a_t)}, \quad (2-6)$$

where  $r_i$  is the distance from the local center of curvature to the tangent point.

---

From Eqs. (2-5) and (2-6) it follows that both the bending angle profile and the real refractivity profile must be evaluated before the imaginary refraction index profile can be computed. The physics behind this is that the bending angle and the real refraction index are related to the ray paths whereas the imaginary refraction index is related to the absorption along these ray paths - and, obviously, the ray path must be known in order to invert the ray amplitude profile.

It is also worth to notice that the measured ray amplitude,  $A_{RX}$ , may be scaled with any arbitrary constant without affecting the results of the integral in Eq. (2-6). The reason for this is that the signal absorption is related to the relative variations in the signal intensity and not the absolute variations. Consequently, there will be no need for calibration of the measured amplitudes as the observations will not be affected by long-term drifts in the instrument, which makes the technique very suitable for climate monitoring.

From the discussion above it follows that for a spherically symmetric atmosphere the complex refraction index profile can be derived from a profile of bending angles and a profile of ray amplitudes. However, the amplitude of a measured RO signals will not only be subject to modulations caused by absorption but will also suffer from amplitude modulations caused defocusing/focusing and spreading due to divergence/convergence of the rays [*Kursinski et al., 1997; Kursinski et al., 2002; Sokolovskiy, 2000; Leroy, 2001a, Jensen et al., 2003a*]. Consequently, the measured amplitudes must be corrected for amplitude modulations caused by spreading and defocusing/focusing before the ray amplitude profile can be computed. For a given frequency, computation of the complex refraction index profile, therefore, follows five different processing steps:

1. Computation of the ray trajectories, which is equivalent to computing bending angle profile as a function of ray impact parameter.
2. Correction for unwanted amplitude modulations (i.e., defocusing/focusing and divergence/convergence of the rays).
3. Computation of the absorption along each ray trajectory, which is equivalent to computing the ray amplitude as a function of impact parameter.
4. Inversion of the bending angle profile into a real refractivity profile.
5. Inversion of the ray amplitude profile into imaginary refractivity profile.

The specific implementation of the different steps depends on the retrieval technique used to compute the bending angle and the ray amplitude profiles. The reader should consult [*Nielsen et al. 2003*] for an overview of how the most common retrieval techniques can be used to retrieve complex refraction index profiles.

In the following it will be described how the FSI technique can be used to compute complex refraction index profiles from a LEO-LEO link. As will be clear from the next sections, the FSI technique has a number of advantages, which makes this technique very suitable for LEO-LEO measurements: 1) it works in multipath zones, 2) defocusing is automatically accounted for, 3) it has high vertical resolution, 4) it does not require a coordinate transformation to fix the transmitting satellite.

For LEO-LEO observations it is a particular advantage that the FSI technique does not require a coordinate transformation to fix the transmitter, which for instance is the case for the canonical transform and the back-propagation techniques [*Gorbunov, 1996; Kursinski et al., 2000; Gorbunov, 2002a*]. This is not a particular problem in traditional GPS-LEO occultations as the movement of the GPS satellite during an

occultation is relatively small allowing for an approximate coordinate transformation to a coordinate system where the GPS satellite is fixed [Gorbunov, 1996; Kursinski *et al.*, 2000]. However, in LEO-LEO occultations the movement of the transmitting satellite is somewhat larger and it may therefore be necessary to use more advanced, and thus more CPU demanding, algorithms in order to achieve the desired accuracy in the required coordinate transformation.

### 3 Application of FSI in a LEO-LEO Link

When the FSI technique is applied to radio occultation signals both bending angles and signal attenuations are automatically assigned to the corresponding impact parameters - also in multipath regions. This property makes the FSI technique very suitable for inversion of LEO-LEO cross-link measurements - also when calibration frequencies are used. The full spectrum inversion method is similar to the canonical transform in the sense that it uses the complex signal received during the whole occultation (synthetic aperture) and thus allows for sub-Fresnel resolution [Gorbunov *et al.*, 2003]. Both methods apply some Fourier integral operator (simply Fourier transform for FSI) and use the derivative of the phase after this transformation. Whereas the output from CT is bending angle and impact parameter, time and instantaneous frequency is the output from FSI – also in case of multipath, where there will be more frequencies to a given time. The Fourier amplitudes describe the distribution of energy with respect to impact parameter in the absence of signal spreading and absorption, and resemble the CT amplitudes.

When using full spectrum inversion to invert radio occultation data, a distinction between ideal occultations and realistic occultations must be made. Here ideal occultations are defined as occultations with a spherical Earth and perfect circular orbits lying in the same plane, whereas realistic occultations are defined as occultations with an oblate Earth and approximately circular orbits lying in two different planes. In the former case, a global Fourier transform can be applied directly to the measured signal; and pairs of ray arrival time,  $t_0$ , and ray Doppler angular frequency,  $\omega_0$ , are related through [Jensen *et al.*, 2003]:

$$(t_0, \omega_0) = \left( -\frac{d \arg(F(\omega_0))}{d\omega}, \omega_0 \right), \quad (3-1)$$

where  $F(\omega)$  represents the Fourier transform of the measured signal. Subsequently, the corresponding bending angle profile is readily computed from the geometry of the occultations by simultaneously solving the following set of equations (for details see e.g. [Jensen *et al.* 2003]):

$$\omega(t) = ka \frac{d\theta}{dt}. \quad (3-2)$$

$$\alpha = \theta + \phi_{TX} + \phi_{RX} - \pi, \quad (3-3)$$

$$a = r_{RX}\sin(\phi_{RX}) = r_{TX}\sin(\phi_{TX}), \quad (3-4)$$

in which:

- $\alpha$  is bending angle.
- $\omega$  is the time derivative of the signal phase in radians.
- $t$  is time.
- $k$  is the wave number.
- $r_{TX}$  is the distance from centre of curvature to the transmitter satellite.
- $r_{RX}$  is the distance from centre of curvature to the receiver satellite.
- $a$  is the ray impact parameter.
- $\theta$  denotes the angle between the two radius vectors.
- $\phi_{TX}$  is the angles between the ray path and the satellite radius vector at the transmitter satellite.
- $\phi_{RX}$  is the angles between the ray path and the satellite radius vector at the receiver satellite.

Equation (3-2) describes the Doppler shifts in the transmitter frequency measured at the receiver produced by the projection of the spacecraft velocity onto the ray path, whereas equations Eqs. (3-3) and (3-4) are geometrical relations (see Figure 2-1). The amplitude of the Fourier transformed field is given by:

$$|F(\omega)| = A_{RX}S, \quad (3-5)$$

in which  $S$  represents amplitude modulations caused by spreading of the signal and may be expressed as [Jensen *et al.*, 2003a; Nielsen *et al.*, 2003]:

$$S = \frac{1}{\sqrt{2\pi k}} \left[ \frac{1}{\left(\frac{d\theta}{dt}\right)^2 r_G r_L \sqrt{1 - \left(\frac{a}{r_G}\right)^2} \sqrt{1 - \left(\frac{a}{r_L}\right)^2}} \right]^{\frac{1}{2}} \left[ \frac{a}{r_G r_L \sin(\theta)} \right]^{\frac{1}{2}}. \quad (3-6)$$

In Eq. (3-6) the first square bracket accounts for amplitude modulations caused by spreading within the occultation plane whereas the last term accounts for spreading in the transverse direction. From Eq. (3-5) the ray amplitude vs. impact parameter profile is readily computed using the ephemeris data and the direct relation between ray Doppler frequency and impact parameter.

In realistic occultations unwanted frequency variations are introduced in the RO signal due to variations in satellite radii and higher order variations in the opening

---

angle,  $\theta$ . These frequency variations must be removed prior to the application of a Fourier transform [Jensen *et al.*, 2003a]. This can be done by a re-sampling of the occultation signal and ephemeris data with respect to  $\theta$ , and by removing frequency variations caused by radial variations in the radius vectors as described by [Jensen *et al.*, 2003a]. For realistic orbits it may also be necessary to account for variations in the satellite radii when correcting for signal spreading, as described by [Gorbunov, 2003]. The purpose of this study is to demonstrate how errors caused by Gibb's phenomenon and noise can be reduced when the FSI technique is applied. We have therefore restricted this study to ideal orbits where the FSI technique can be implemented directly as a Fourier transform though it should be stressed that our results are valid also for realistic orbits and, with minor modifications, for other Fourier Operator based techniques as well.

## 4 Analysis of Gibb's Phenomenon

The Fourier transform, like other Fourier operators, of a RO signal will suffer from Gibb's phenomenon [Proakis and Manolakis, 1996], also known as ringing. Gibb's phenomenon occurs because RO signals always have finite duration and cause artificial oscillations in phase and amplitude. Consequently, Eqs. (3-1) and (3-4) are only approximate for real RO signals. The artificial oscillations in the Fourier phase are generally small compared to phase variations induced by the atmosphere and the resulting relative errors in the derived bending angle profile are very small (see e.g. [Jensen *et al.*, 2003a]). This explains why Fourier operator based methods are so efficient in retrieving bending angle profiles in spite of the inherent problem of Gibb's phenomenon. Unfortunately, the same is not true when it comes to the amplitude of the transformed field. In this case the artificial oscillations caused by ringing are in the same order of magnitude as the amplitude variations caused by atmospheric absorption. This is illustrated in Figure 4-1 below showing an example of the FFT of a simulated 10 GHz RO signal for a model atmosphere with exponential decaying real and imaginary refractivities. Details regarding our simulations will be given Section 7.

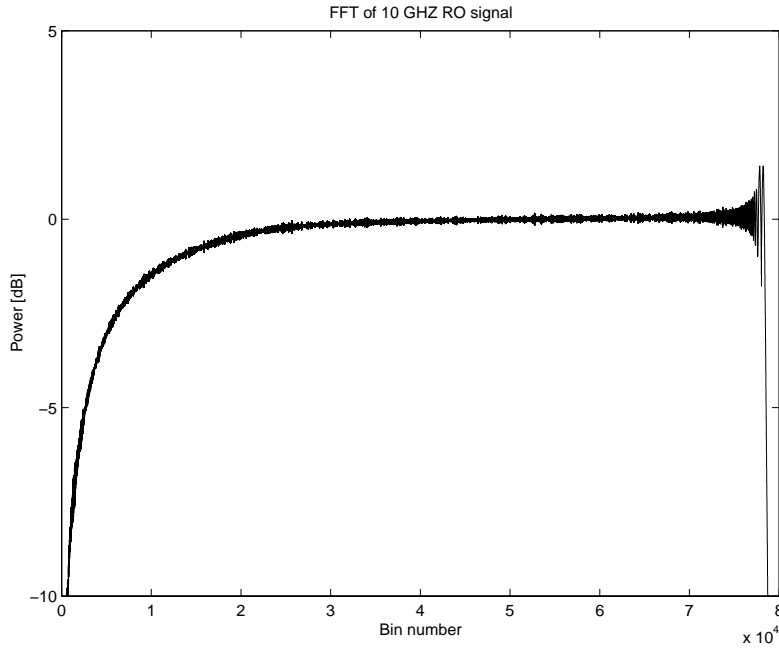


**Figure 4-1:** Example of FFT of a simulated 10 GHz RO signal with absorption. This power spectrum has both a smooth variation due to atmospheric absorption and rapid oscillations caused by ringing.

Artificial noise caused by Gibb's phenomenon is amplified in the retrieval chain as the ray amplitude enters the Abel integral Eq. (2-6), as a derivative. If not properly dealt with these oscillations may therefore result in a very noisy profile of imaginary refractivity. In the following paragraph we will show how ringing can be significantly reduced by applying window functions to the Fourier transform.

The FSI technique is derived from the method of *stationary phase* and relies on the assumption that the ray phase variations can be locally approximated by a second order polynomial. Before describing how window functions can be applied to real RO signals, it is therefore instructive to first consider a simplified model of a RO signal described by constant amplitude and pure quadratic phase variation, in order to get a better understanding of how the final durations of a measured RO signal affects the corresponding Fourier transform.

Now, consider the very simple case of a constant amplitude chirp signal:

$$s(t) = A \exp(i\pi\beta t^2). \quad (4-1)$$

The Fourier transform of this signal yields [Goodman, 1996]:

$$F(\omega) = \int_{-t_0}^{t_0} s(t) \exp(i\omega t) dt = \frac{A}{\sqrt{2\beta}} \exp\left(-i \frac{\omega^2}{4\pi\beta}\right) \int_{v_0}^{v_1} \exp\left(i \frac{\pi v^2}{2}\right) dv, \quad (4-2)$$

in which:

---


$$v = \sqrt{2\beta} \left( t - \frac{\omega}{2\pi\beta} \right), \quad v_0 = -\sqrt{2\beta} \left( t_0 + \frac{\omega}{2\pi\beta} \right), \quad v_1 = \sqrt{2\beta} \left( t_0 - \frac{\omega}{2\pi\beta} \right). \quad (4-3)$$

This expression may be rewritten in terms of the Fresnel cosine,  $C(x)$ , and the sine,  $S(x)$ , integrals:

$$C(x) = \frac{1}{\sqrt{2}} \int_0^x \cos\left(\frac{\pi v^2}{2}\right) dv, \quad S(x) = \frac{1}{\sqrt{2}} \int_0^x \sin\left(\frac{\pi v^2}{2}\right) dv, \quad (4-4)$$

and the Fourier transform given by Eq. (3-5) may therefore be written as:

$$F(\omega) = \frac{A}{\sqrt{\beta}} \exp\left(-i \frac{\omega^2}{4\pi\beta}\right) \left[ C(v_0) - C(v_1) + i(S(v_0) - S(v_1)) \right] \quad (4-5)$$

where the terms in the square brackets describe two so-called *Cornu spirals* known from diffraction theory, see e.g. [Born and Wolf, 1996]. The terms in front of the square bracket in Eq. (4-5) are independent of the length of the time series revealing that for a chirp signal the artificial oscillations in the Fourier transform are governed by Fresnel integrals. Hence, convergence of the Fourier transform is related to the convergence of the Fresnel integrals expressed as a chirp integral:

$$CS(x) = C(x) + iS(x) = \frac{1}{\sqrt{2}} \int_0^x \exp\left(i \frac{\pi v^2}{2}\right) dv, \quad (4-6)$$

This integral is characterised by having an oscillatory nature and a slow convergence with increased  $x$ . This is illustrated in Figure 4-2 showing the magnitude of  $CS(x)$  and in Figure 4-3 depicting the Cornu spiral plotted as the imaginary part of  $CS(x)$  as function of its real part for same range of  $x$  values shown in Figure 4-2.

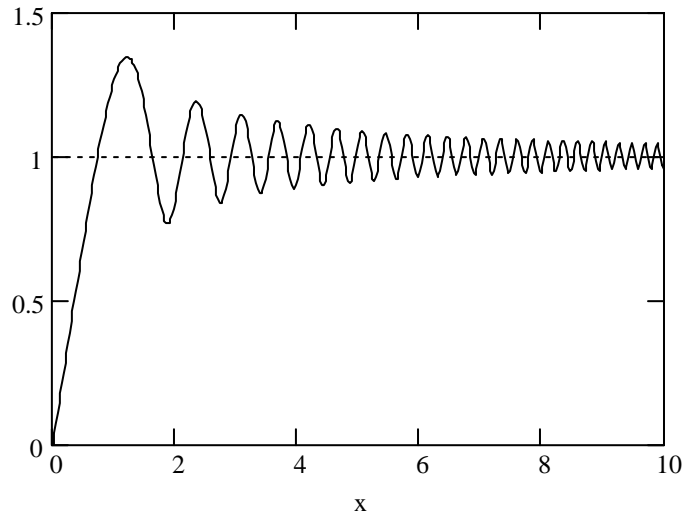


**Figure 4-2:** Solid line: amplitude of chirp integral,  $CS(x)$ , as a function of  $x$ . Dashed line: limiting value of chirp integral,  $|CS(\infty)|$ .

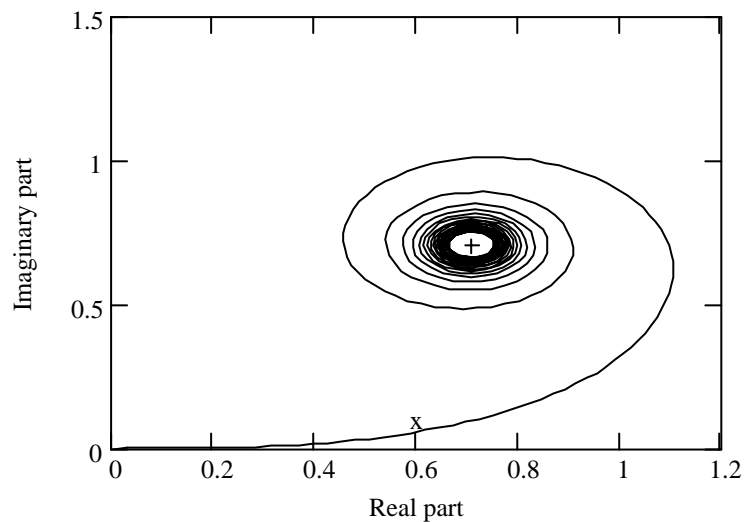


**Figure 4-3:** Solid curve: Cornu spiral – plotted as real part of chirp integral vs. imaginary part of chirp integral for  $x \in [0;10]$ . Cross: limiting value for  $x \rightarrow \infty$ .

From Figure 4.2 it can be seen that major contribution to the limiting value,  $|CS(\infty)|$ , comes from the interval  $0 \leq x \leq 1.5$  whereas the remaining part of the integration is merely used to damp the oscillations. It therefore seems intuitively clear that the convergence of the chirp integral can be sped up by applying an appropriate window function centered on  $x=0$ , i.e.

$$CS_w(x) = \frac{1}{\sqrt{2}} \int_0^x w(v) \exp\left(i \frac{\pi v^2}{2}\right) dv \approx CS(\infty) \quad (4-7)$$

In order to effectively damp the oscillations the window function,  $w(x)$ , should exhibit a smooth transition from a maximum value at  $v=0$  to zero at  $v=x$ . For this study the three term Blackman-Harris window has been found to work well. This specific window function was chosen as it has very low side lobes, which damps ringing, and yields a low reduction in the signal to noise ratio (SNR), [Harris, 1978]. The three term Blackman-Harris window is defined by:

$$w(v, \Delta v) = a_0 - a_1 \cos\left(2\pi \frac{v + \Delta v}{2\Delta v}\right) + a_2 \cos\left(4\pi \frac{v + \Delta v}{2\Delta v}\right), \quad (4-8)$$

in which  $\Delta v$  is the window length and  $a_0 = 0.44959$ ,  $a_1 = 0.49364$ ,  $a_2 = 0.05677$ . When this window is applied to the chirp integral convergence is sped up significantly for both phase and amplitude as compared to the original chirp integral. This is illustrated in Figure 4-4 and Figure 4-5 which are identical to Figure 4-2 and Figure 4-3, respectively, except that results for the windowed chirp integral have been added.

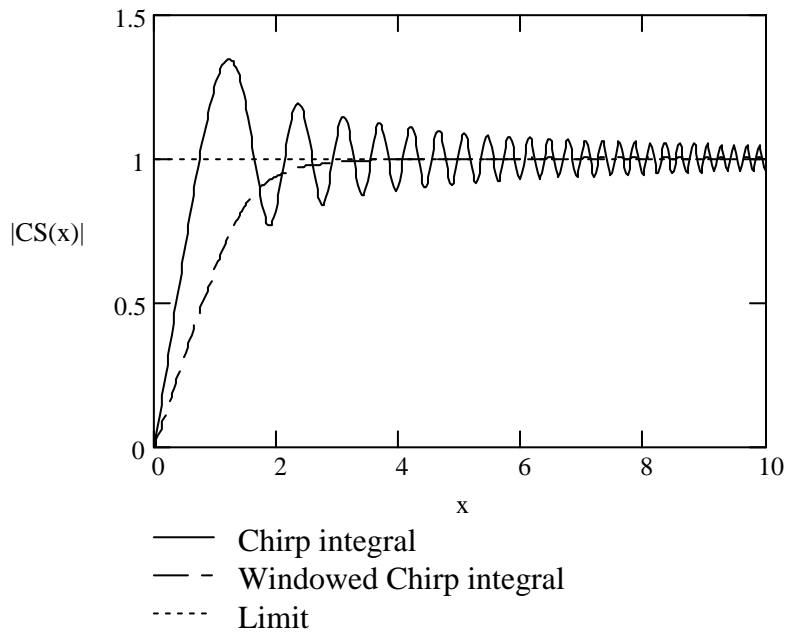


**Figure 4-4:** Same as Figure 4-2 except that results for windowed chirp integral have been added. Solid line: amplitude of chirp integral,  $CS(x)$ , as a function of  $x$ . Dashed line: amplitude of windowed chirp integral  $CS_w(x)$ . Dotted line limiting value of chirp integral,  $|CS(\infty)|$ .

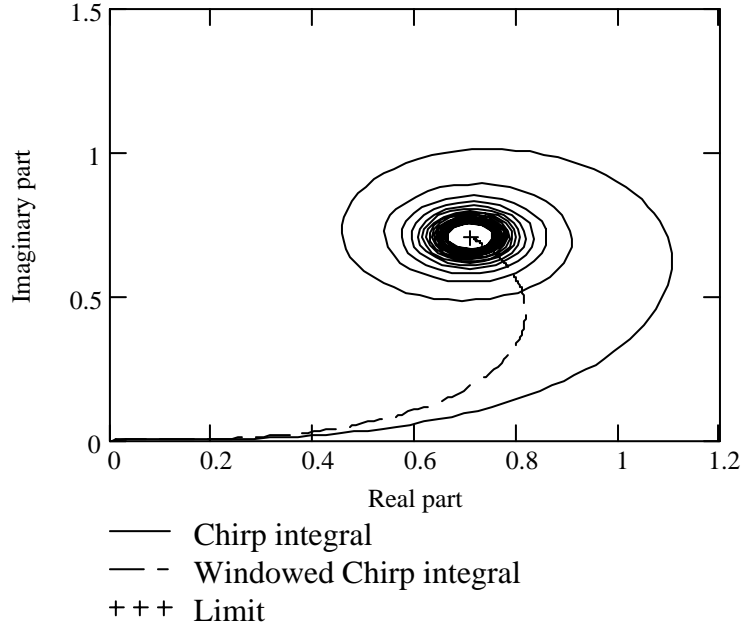


**Figure 4-5:** Same as Figure 4-3 except that results for the windowed chirp integral have been added. Solid curve: Cornu spiral – plotted as real part of chirp integral vs. imaginary part of chirp Integral for  $x \in [0;10]$ . Dashed curve: windowed chirp integral plotted in the same way as the Cornu spiral. Cross: limiting value for  $x \rightarrow \infty$ .

## 5 Windowed FSI

From the discussion and analysis in the foregoing section it is clear that the convergence of a chirp integral can be sped up by applying an appropriate window function. We will now apply this result in order to reduce ringing in the Fourier transform of a real RO signal.

Application of a window function to the Chirp integral is relatively simple as the window is always centered on  $x=0$ , however, if window functions are to be used with the Fourier integral in Eq. (4-2) the window functions must be centered around the time,  $t_c$ , corresponding to  $v(t_c) = 0$ . From Eq. (4-3) it follows that this point in the observed time series is given by:

$$t_c = \frac{\omega}{2\pi\beta} \quad (5-1)$$

For ideal satellite orbits and a spherically symmetric atmosphere each ray Doppler frequency only occurs once during an occultation [Jensen et al., 2003a]. Hence, from Eqs. (4-1) and (5-1) it follows that the window must be placed around the point in the time series where the ray with Doppler frequency,  $\omega$ , arrived at the receiver,

corresponding to stationary phase point of the Fourier integral [Jensen et al., 2003a]. In this case the Fourier integral may be written as:

$$F(\omega) = \int_{-\frac{\Delta t}{2}}^{\frac{\Delta t}{2}} w(t-t_c, \Delta t) s(t) \exp(i\omega t) dt, \quad (5-2)$$

assuming that  $-t_0 < -\frac{1}{2}\Delta t + t_c$  and  $\frac{1}{2}\Delta t + t_c < t_0$ , where  $\Delta t$  is the length of the window function.

The question is now; what is the best choice of window length? Clearly by using a long window we will get a long synthetic aperture and thus a high vertical resolution [Gorbunov et al., 2003]. Also, the results in Figures 4-4 and 4-5 suggest that the window should be as long a possible in order to assure the best convergence. This would also have been the case if RO signals were pure chirp signals, however, RO signals are not chirp signals and, in contrast to chirp signals, they do not have constant amplitude and linear Doppler variation. Nevertheless, within a limited time interval RO signals can be well approximated by a chirp. In multipath regions this approximation is valid for each single path signal, but not for the combined signal, which is sufficient for our purpose as the contribution to the Fourier integral only comes from one single path namely the path containing the given Fourier frequency. From that perspective the window length should be as short as possible in order ensure that the signal can be well approximated by a chirp within the duration of the window function.

Another drawback of using a very long window is that it will decrease the signal to noise ratio of the transformed field as the noise power is proportional to the window length whereas the signal power,  $|F(\omega)|^2$ , is almost independent of the length of the window if the window is sufficiently long (see Figure 4-4). Also the influence of tracking errors is expected to increase with increasing window length simply because the likelihood of the occurrence of a tracking error within the duration of a window obviously increases as the window length increases. This seems to suggest that we choose a very short window, however, from Figure 4-4 and Figure 4-5 it can be seen that if the window is chosen to be too short both phase and amplitude of the transformed field will be biased. Consequently, the choice of window length is a trade off between the different effects described in the foregoing discussion. For this study we haven chosen to use a window length of  $x = 3$  in Figure 4-4, corresponding roughly to the shortest bias free window. From Eq. (4-3) it follows that the equivalent duration of the window is given by:

$$\Delta t = \frac{6}{\sqrt{2|\beta|}}, \quad \beta = \left. \frac{1}{2\pi} \frac{d\omega}{dt} \right|_{t=t_c}, \quad (5-3)$$

showing that the window length is proportional to the inverse square root of the Doppler frequency variations. As real RO signals are not chirp signals  $\beta$  is not a constant but represents the second derivative of the ray phase equivalent to the

---

variations in the ray Doppler frequency.  $\beta$  may also be calculated directly from the Fourier Spectrum, using Eq. (3-1) as:

$$\beta = \frac{1}{2\pi} \frac{d\omega}{dt} \Big|_{t=t_c} = -\frac{1}{2\pi} \left( \frac{d^2 \arg(F(\omega))}{d^2 \omega} \right)^{-1} \quad (5-4)$$

When the length of the window function is determined according to Eq. (5-3), long windows will be assigned to frequencies related to areas in the atmosphere with large gradients in the real refractivity whereas short windows will be assigned to frequencies related to atmospheric regions where the refractivity profile is smooth. This is a consequence of Eq. (5-3), as a slow variation in the ray Doppler frequency (strong defocusing) corresponds to large gradients in the atmosphere, whereas rapid variations in the Doppler frequency correspond to smooth refractivity variations.

From Eqs. (5-1) and (5-3) it follows that application of the windowed Fourier transform requires a priori knowledge of the temporal variation in the ray Doppler frequency in order to determine the correct position and duration of the different windows. This makes application of the method to arbitrary signals rather complicated. Fortunately this is a surmountable problem for RO occultations signals as the Doppler frequency variation can be determined using standard RO retrieval schemes e.g. FSI or canonical transform. It means that we can exploit the fact, in spite of Gibb's phenomenon, that the ray Doppler frequency variation can be determined accurately using any known standard Fourier operator method, which allows for the determination of the window functions. This principle is illustrated in Figure 5-1.

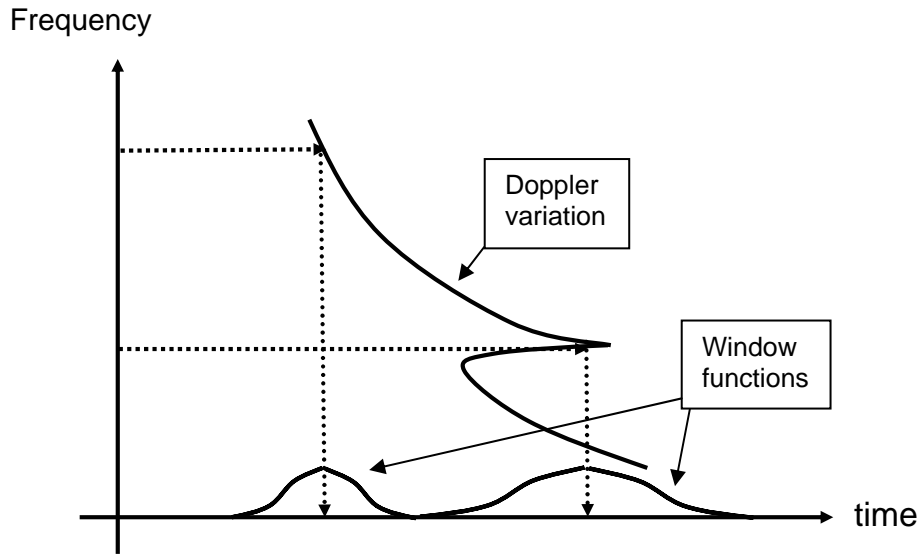


**Figure 5-1:** Principles of windowed FSI: position and durations of window functions are determined for each frequency from the frequency variations predicted by a standard FSI. Long windows are applied when the ray Doppler frequency exhibit slow variations whereas short windows are applied when the ray Doppler frequency has rapid variations.

Subsequently, the windowed transformation is performed reducing ringing in the amplitude of the transformed field which can then be used for accurate absorption measurements. At this point it is advantageous also to recalculate the bending angle profile based on the windowed transformation to get rid of the small oscillations from ringing in the phase of the original transformation. Furthermore, this will also reduce the impact of noise as the windowed transformation is not based on the entire time series but only on some fraction of the time series and it is therefore less sensitive to noise than the original transformation. The influence of noise on the windowed transformation is analysed later in this section. Based on the foregoing discussion it is evident that application of a windowed FSI to real occultation signals must follow the steps listed below:

1. Use standard FSI to compute ray Doppler frequency variation.
2. Compute window lengths and positions from the Doppler variation using Eqs. (5-1) and (5-3).
3. Re-compute the Fourier spectrum using the derived windows functions.
4. Compute refraction and transmission profiles from the new Fourier Spectrum.

In principle the last three steps could be repeated in an iterative manner which would also allow for compensation of absorption in the windowed Fourier transform. This approach has not been tried by the authors as our current experience with the method indicates that one iteration is sufficient. Furthermore, additional iterations will also increase computation time which is not desirable as the single iteration approach is already demanding in terms of CPU power because the windowed Fourier transformations cannot be implemented as a FFT. However, if the signal experiences

very rapid amplitude variations due to absorption, additional ringing could be generated, in this case further iterations might be necessary.

Figure 5-2 shows a comparison between the amplitude of a FFT of a simulated RO signal compared to the amplitude of the corresponding windowed Fourier transform. The simulated signal is the same as the one used in Figure 4-1 and corresponds to a 10 GHz RO signal which has traversed a spherically symmetric atmosphere with exponential decaying real and imaginary refractivity. The figure clearly demonstrates that the windowed Fourier transform significantly reduces Gibb's phenomenon in the Fourier transform.

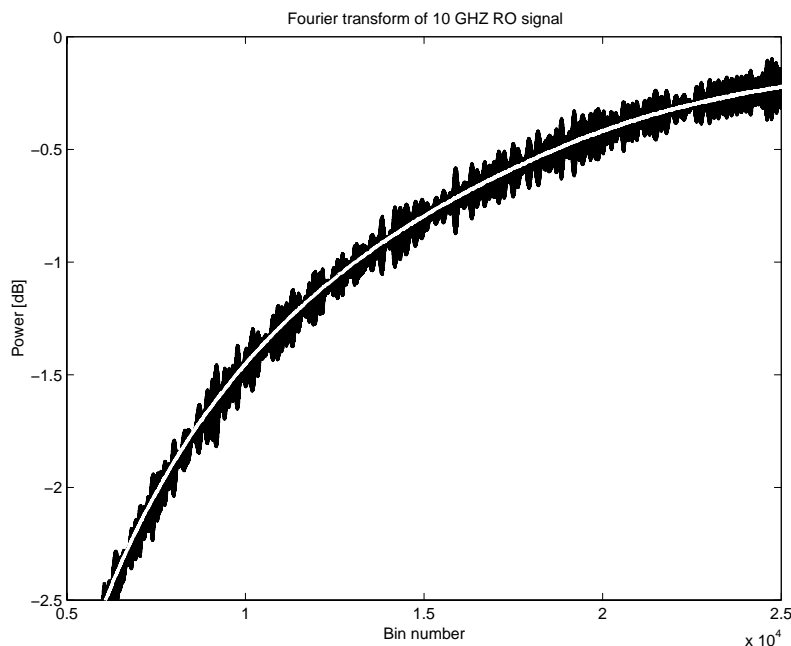


**Figure 5-2:** Comparison between FFT power spectrum, noisy black curve, and power spectrum of the windowed Fourier transform (white curve). The figure is a close-up of Figure 4-1 with the addition of the power spectrum computed using the windowed Fourier transform.

## 6 Noise Impact

Due to the applied window functions the WFSI will be less sensitive to noise than the standard FSI. This is best illustrated by considering the windowed Fourier transform of a RO signal with additive white noise  $n(t)$  with noise power  $\sigma_n^2$ :

$$\begin{aligned}
F(\omega) &= \int_{-\frac{\Delta t}{2}}^{\frac{\Delta t}{2}} w(t-t_c, \Delta t) (s(t) + n(t)) \exp(i\omega t) dt \\
&\approx F_t(\omega) + \int_{-\frac{\Delta t}{2}}^{\frac{\Delta t}{2}} \exp(i\omega t) w(t-t_c, \Delta t) n(t) dt,
\end{aligned} \tag{6-1}$$

in which  $F_t(\omega)$  is the true value of the Fourier transform in the absence of noise and ringing. The corresponding signal to noise ratio of the transformed fields is:

$$SNR_{WFSI}(\omega) = \frac{|F_t(\omega)|^2}{\sigma_n^2 \int_{-\frac{\Delta t}{2}}^{\frac{\Delta t}{2}} w(t-t_c, \Delta t)^2 dt}, \tag{6-2}$$

when  $\Delta t$  satisfies Eq. (5-3). For the three term Blackman-Harris window Eq. (6-2) yields:

$$SNR_{WFSI}(\omega) = \frac{|F_t(\omega)|^2}{0.3\sigma_n^2\Delta t} = \frac{A_{RX}^2 S^2}{0.3\sigma_n^2\Delta t}, \tag{6-3}$$

in which the constant of 0.3 has dimension of time, [s]. Eq. (6-3) shows that the  $SNR$  of the transformed field is proportional to the inverse of the window length. This implies that for constant background noise the highest signal to noise ratios in the transformed field occur for large impact parameters, i.e., in the upper atmosphere whereas the lowest  $SNR$  will be observed for rays traversing the troposphere where the defocusing is most significant. It also follows from Eq. (6-3) that the  $SNR$  of the windowed Fourier transform is higher than for the normal Fourier transform, even when the artificial noise caused by ringing is ignored as long as the required window length is less than the duration of the measured time series.

From Eq. (6-3) we can also estimate the relative variance of the ray intensity, i.e., the squared amplitude, computed through Eq. (3-4) assuming that the transformed noise is white and using the result in [Nielsen *et al.*, 2003] and Eq. (4-11):

$$(5-4)$$

$$\frac{\sigma_{I_{RX}}^2}{A_{RX}^2} \approx \frac{4}{S^2} \frac{|F_t(\omega)|^2}{A_{RX}^2 SNR_{WFSI}} = \frac{1.2\sigma_n^2 \Delta t}{(SA_{RX})^2} = \frac{12.8}{S^2 SNR_0 \sqrt{\left| \frac{d\omega}{dt} \right|}},$$

where  $SNR_0$  is the signal to noise ratio of the measured signal in the absence of absorption, spreading, and defocusing.

At this point it is relevant to compare this result with the corresponding variance of the ray intensity calculated based on GO processing. When GO is applied the ray Doppler frequency is computed as the instantaneous frequency of the measured signal which allows for computation of the bending angle profile, see e.g. [Kursinski *et al.*, 2000], whereas the ray amplitude is computed directly from the measured amplitude as [Leroy, 2001a and Nielsen *et al.* 2003]:

$$A_{RX}^2 = \frac{|s|^2}{S^2 \left| \frac{d\omega}{dt} \right|}, \quad (6-5)$$

where the term  $|d\omega/dt|$  correct for the defocusing, as we have assumed that the satellite orbits are perfectly circular (see [Jensen *et al.*, 2003a]). The relative variance of this estimate is:

$$\frac{\sigma_{I_{RX}}^2}{A_{RX}^2} \approx \frac{4}{S^2 SNR_0 \left| \frac{d\omega}{dt} \right|}. \quad (6-6)$$

Eqs. (6-4) and (6-6) implies that the windowed FSI estimate will only be less sensitive to additive noise than the GO estimate when the signal experience strong defocusing. However, it should be noted that the estimate given by Eq. (6-5) will have larger variance than predicted by Eq. (6-6) as there will also be a contribution from the error in the estimate of the defocusing factor,  $|d\omega/dt|$ , which could be rather large at low  $SNR$ . Furthermore, GO processing cannot handle multipath and the resolution is limited to the size of the first Fresnel zone. On the other hand GO offers a simple implementation and requires only moderate computer power. Consequently, for operational applications the GO approach should be used above the troposphere where defocusing is weak (high  $SNR$ ) and the atmosphere is relatively smooth, whereas the windowed FSI should be applied in the troposphere where the atmosphere have many small scale structures causing multipath propagation and strong defocusing.

## 7 Windowed FSI of Simulated RO Signals

In this section the WFSI technique is applied to a simulated LEO-LEO radio occultation signal and its performance is compared to the performance of the traditional FFT implementation of the FSI technique. The simulated satellite system consists of two counter rotating satellites orbiting the Earth in the same plane. The transmitter is at a height of 850 km and the receiver is deployed at 650 km, which is also chosen as the baseline in the ACE+ project. For this study we only consider a 10 GHz signal, but the authors have found similar results when using 17 GHz and 23 GHz signals.

The simulated signal was generated as a solution to the parabolic approximation of the Helmholtz wave equation computed using the split-step algorithm, also known as the multiple phase-screen technique [Benzon *et al.*, 2002]. Propagation from the last screen to the LEO orbit is calculated using the Fresnel diffraction integral. The satellite orbits used in all the simulations are perfectly circular lying in the same plane and the simulated atmosphere is spherical symmetric. The simulated signal is amplitude and excess phase sampled like real radio occultation signals. Before a signal can be processed using either FSI or WFSI, the total signal phase has to be reconstructed in order to restore the ‘original’ signal. This is done by frequency shifting the signal to base band, followed by up-sampling of the signal through interpolation of the amplitude and the new phase. When the signal is interpolated, the sampling rate must correspond to at least twice the new signal bandwidth in order to satisfy the sampling theorem.

The simulated RO signal was based on an atmosphere described by a known real refractivity profile expressed as:

$$N(h) = 315 \exp\left(\frac{-h}{7.35\text{km}}\right) + B \exp\left(\frac{-(h-BH)^2}{0.05\text{km}^2}\right) \quad (7-1)$$

This refractivity profile represents an exponential with a Gaussian shaped bump. In Eq. (7-1)  $BH$  is the height of the bump, and  $B$  determines the size of this bump. The first term in the equation is the refractivity of the reference atmosphere defined by the International Telecommunications Union [ITU, 1981]. The second term in the equation determines the strength and height of the refractivity bump. Such a bump in the refractivity profile can be used to simulate multipath effects. The duration of a possible multipath situation is determined by the magnitude of the parameter  $B$ . In the simulations,  $B$  and  $BH$  have been set to 15 and 3 km, respectively, which yields an atmosphere with significant gradients leading to multipath propagation.

The imaginary refractivity index,  $n''$ , is described by:

$$n'' = \kappa n' \quad (7-2)$$

In this study  $\kappa$  is constant and equal to  $3 \times 10^{-5}$ . For the WFSI retrieval a minimum window length was imposed in order to ensure that the maximum resolution was limited by diffraction to approximately 20 m. This diffraction limit was calculated

using the formulas presented in [Gorbunov *et al.*, 2003] and guarantees that no hidden smoothing is introduced by using the windowed Fourier transform. The simulated signal was sampled at 700 Hz. The amplitude variation of this signal is depicted in Figure 7-1 below which clearly shows multipath interference in the interval from 23 sec to 33 sec.

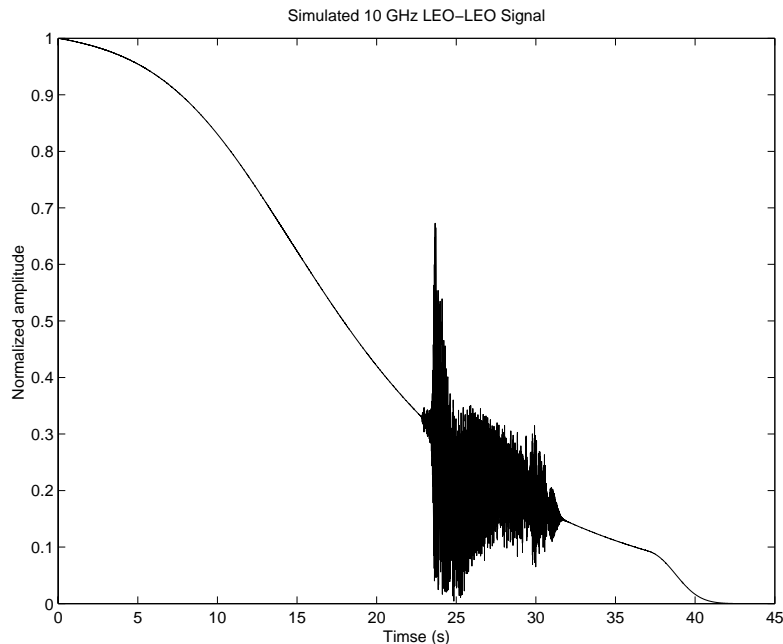


**Figure 7-1:** Amplitude variations of simulated LEO-LEO signal.

The FSI and the WFSI were applied to this signal in order to derive bending angle profiles and profiles of optical depth,  $\tau$ . The optical depth is related to ray amplitude through:

$$\tau = -2 \ln \left( \frac{A_{RX}}{A_{TX}} \right) \quad (7-3)$$

Figure 7-2 shows a comparison between the bending angle profiles retrieved from the simulated signal using FSI and WFSI as well as the true bending angle profile computed as the Abel transform of Eq. (7-1). The Figure shows that both methods are capable of retrieving the bending angle profile also in the multipath zones. However, the figure also reveals that the bending angle profile computed using the standard FSI suffers from small oscillations caused by Gibb's phenomenon in the Fourier spectrum whereas these oscillations are significantly reduced in the bending angle profile computed from the WFSI. In the retrieval of the FSI and WFSI profiles no smoothing has been applied and the derivatives of the Fourier spectra have been computed simply as a two point differentiation. However, it should be noticed that for practical implementation the performance of both techniques can be improved by using some kind of smoothing. Smoothing was not applied in this study since the purpose of the figure is to compare the raw methods - application of any smoothing will just blur the comparison.

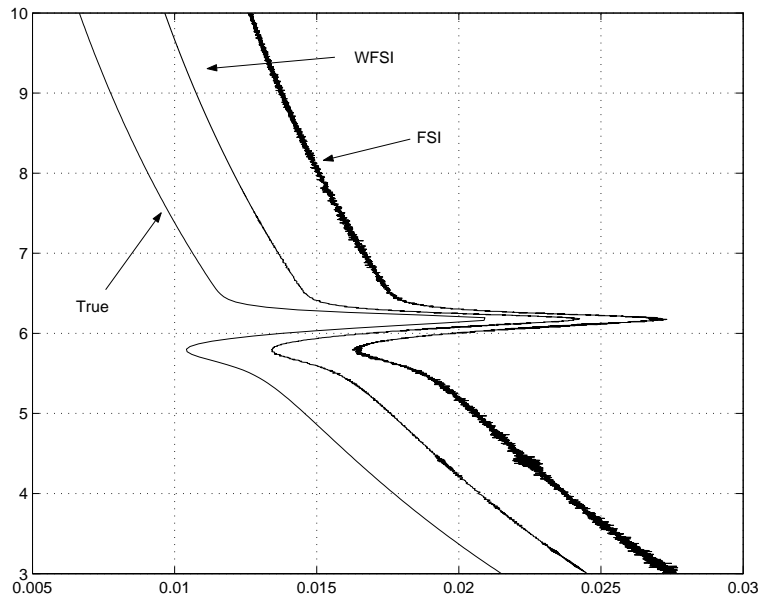


**Figure 7-2:** *Noise free signal - comparison between the true bending angle profile and the corresponding profiles retrieved using FSI and WFSI. The FSI and the WFSI profiles are displaced respectively 0.003 radians and 0.006 radians relative to the true profile.*

Figure 7-3 compares the retrieved raw profiles of optical depth with the true profile computed using Eqs. (2-4) and (7-2). It follows from the figure that the impact of ringing in the optical depth profile is significantly reduced when the WFSI technique is used as compared to the FSI technique. For both the FSI and the WFSI the best performance is found away from the multipath zone whereas the performance of both methods is degraded in the multipath region. The spikes in the FSI profile occur when the oscillations in the ray amplitude cause the ratio  $A_{RX}/A_{TX}$  to be close to zero, see Eq. (7-3).

Figure 7-3 also reveals that both methods have problems in resolving the optical depth in the multipath regions where the methods overestimate the absorption. The bias is believed to be caused by higher order phase variations in the multipath region violating the assumption inherent in both the FSI and the WFSI that the ray phase variations can be locally approximated by a second order polynomial. The reason why the bending angle can be successfully resolved in multipath region is that the relative variations in the phase are much larger than the relative variations in the amplitude. This makes retrieval of bending angles less sensitive to disturbances and noise than retrieval of optical depth. This can also be seen by comparing Figures 7-2 and 7-3, which indicates that the relative impact of ringing is somewhat larger for the bending angle profile than for the optical depth profile.

It is also important to note that the real refractivity is computed as an Abel transform of the bending angle profile (see Eq. 2-5) whereas the imaginary refractivity is computed as an Abel transform of the derivative of the optical depth (see Eq. 2-6). This makes the impact of ringing (and other errors) in the profiles of optical depth far more critical than the impact of ringing in the bending angle profile when geophysical parameters are to be retrieved.

The impact of higher order phase variations may be reduced if calibration tones are used as the bias introduced in the optical depth profiles should be nearly identical for two signals constituting a pair of calibration tones. If the biases in optical depth are

---

identical for two frequencies this bias will cancel out when the difference in optical depth for these two frequencies are computed. Another approach would be to account for the higher order phase terms in the window functions. The authors are currently investigating the latter approach.

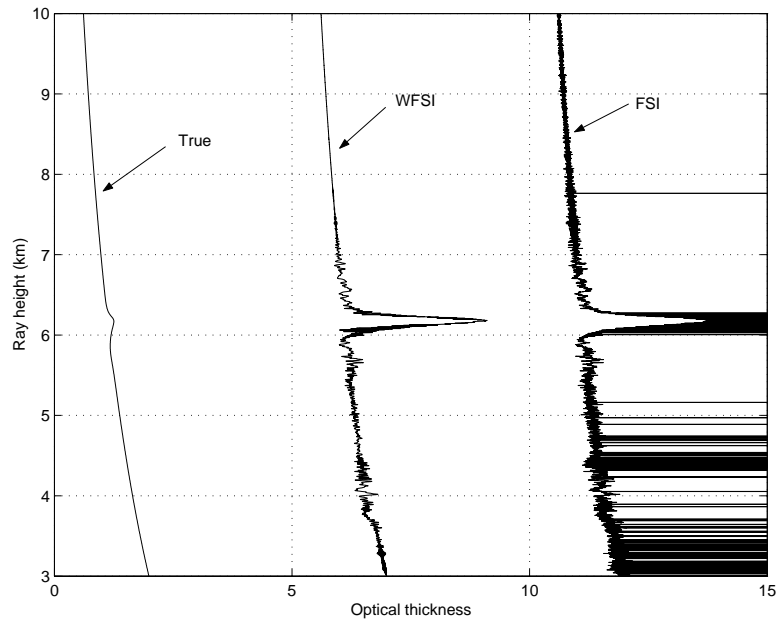


**Figure 7-3:** *Noise free signal - comparison between the true profile of optical depth and the corresponding profiles retrieved using FSI and WFSI. The FSI and the WFSI profiles are displaced respectively by 5 and by 10 relative to the true profile.*

In order to illustrate the superior noise performance of the WFSI as compared to the FSI we now add Gaussian white noise with a noise density of 66 dBHz to the simulated signal and repeat the retrievals. Figure 7-4 below shows a comparison between the two retrieved profiles and the true bending angle profile.

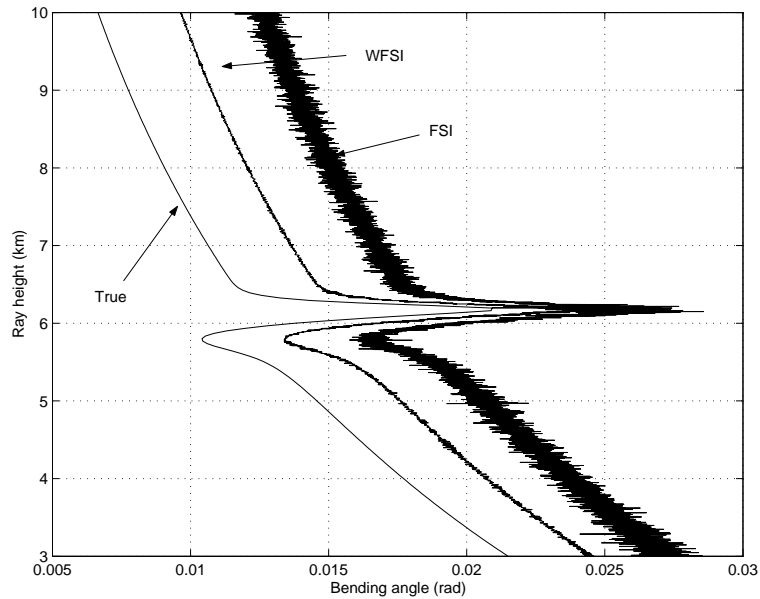


**Figure 7-4:** Noisy signal - comparison between the true bending angle profile and the corresponding profiles retrieved using FSI and WFSI. The FSI and the WFSI profiles are displaced 0.003 radians and 0.006 radians relative to the true profile, respectively.

The figure shows the same trend as was found for the noise free signal, see Figure 7-2, but it also shows that the impact of the noise is far more significant for the standard FSI than it is for the WFSI as predicted by the analysis in the foregoing section. The same conclusion can be drawn from Figure 7-5 depicting a comparison between retrieved profiles optical depth and the true profile for the noisy signal.

As a final remark, it should be noticed that all the results presented in study are ‘raw’ results i.e., no smoothing has been applied in the retrievals. For practical application it would advantageous to apply some kind of noise reducing smoothing, which would obviously improve the performance of both FSI and WFSI. As mentioned earlier, smoothing was not applied, as the purpose of this study has been to compare the raw methods.

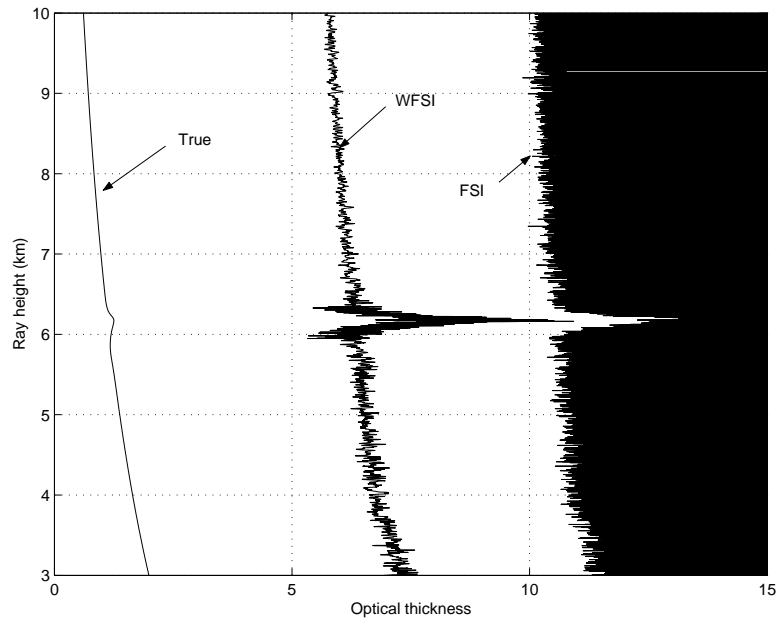


**Figure 7-5:** Noise free signal - comparison between the true profile of optical depth and the corresponding profiles retrieved using FSI and WFSI. The FSI and the WFSI profiles are displaced respectively by 5 and by 10 relative to the true profile.

---

## 8 Summary and Conclusion

When Fourier Operator based methods are applied to radio occultation signals the transformed field will suffer from artificial oscillations caused by Gibb's phenomenon due to the finite duration of RO signals. These artificial oscillations in the transformed field lead to similar oscillations in the retrieved profiles of bending angles and optical depth. RO observations based on absorption, i.e., retrieval of imaginary refractivity are more sensitive to ringing than RO observations of ray bending, i.e., retrieval of real refractivity. The reason for this is that the relative variations in the ray phase induced by the atmosphere are larger than the relative variations in ray amplitude induced by atmospheric absorption.

In this report we have demonstrated how application of window functions to the FSI technique leads to reduced ringing in the transformed field. We refer to the method presented in this report as the windowed FSI (WFSI). The WFSI technique exploits the fact that the major contribution to a given a Fourier component in a RO signal comes from the part of the signal located in the vicinity of the stationary phase point corresponding to that specific Fourier component. The length of the interval, which gives the major contribution to a Fourier component, depends on the derivative of the corresponding ray Doppler frequency. In the WFSI technique window functions of the same form but with different durations are applied to the different Fourier component centered on the corresponding stationary phase points. The duration and position of the individual windows can be determined from a priori knowledge of the variation in the ray Doppler frequency. For practical applications this information can be obtained with sufficient accuracy from a standard FSI.

An analysis of the impact of noise has been carried out and it has been shown that the WFSI is less sensitive to white noise than the standard FSI. Furthermore it is also expected that the WFSI will be less sensitive to tracking than standard FSI though this has not been investigated in this report.

The drawback of the WFSI as compared to FSI is that it is significantly more demanding in terms of computer power because the windowed Fourier transform cannot be implemented as an FFT.

The superior performance of the WFSI as compared to standard FSI has been demonstrated by applying both techniques to simulated radio occultation signals in a LEO-LEO setup. The results from the simulations verify the theoretical findings and showed that both bending angle profiles and profiles of optical depth retrieved using WFSI are less sensitive to ringing and white noise than the corresponding profiles derived from the standard FSI. However it was also found that the retrieved profiles of optical depth were strongly biased in the part of the multipath region associated with the most rapid phase variations. The authors believe that this bias is caused by higher order phase variations violating the assumption inherent in both the FSI and the WFSI technique that these higher order variations are small. Though the simulations were performed for a 10 GHz signal it is expected that the WFSI will also have superior performance compared to the FSI for GPS-LEO occultations, though the impact will not be as significant since the windows will be longer for GPS-signals due the longer wavelength.

In this report the application of window functions was demonstrated only in connection with the FSI technique, however, it is anticipated that the findings in this report can be applied also to other retrieval techniques based on a Fourier operator.



---

## 9 References

**Benzon, H.-H.**, L. Olsen, and A. S. Nielsen, *Analysis and definition of algorithms for an atmospheric wave propagator*. DMI Scientific Report 03-01, 2002.

**Beyerle, G.**, S. Sokolovskiy, J. Wickert, T. Schmidt, and Ch. Reigber, *Atmospheric sounding by GNSS radio occultation: An analysis of the negative refractivity bias using CHAMP observations*. Radio Sci., currently under review, 2003.

**Born, M.** and E. Wolf, *Principles of Optics*, Cambridge University Press, 1999.

**Eriksson, P.**, Jimenez, C., Murtagh, D., Elgered, G., Kuhn, T., Buhler, *Measurement of tropospheric/stratospheric transmission at 10-35 GHz for H<sub>2</sub>O retrieval in low Earth orbiting satellite links*. Radio Sci. Vol. 38, No. 4, 8069  
doi:10.1029/2002RS002638 13 June 2003.

**Eshleman, V.R.**, D.O. Muhleman, P.D. Nicholson, and P.G. Steffes, *Comment on absorbing regions in the atmosphere of Venus as measured by radio occultation*. Icarus, 44, 793-803, 1980.

**Goodman, J. W.**, *Introduction to Fourier optics*, The McGraw-Hill, Inc. 1996.

**Gorbunov, M.E.**, A.S. Gurvich and L. Bengtsson, *Advanced algorithms of inversion of GPS/MET satellite data and their application to reconstruction of temperature and humidity*, Tech. Rep. 211, Max-Planck-Institute for Meteorology, Hamburg, 1996.

**Gorbunov, M.E.**, and A.S. Gurvich, *Algorithms of inversion of Microlab-1 satellite data including effects of multipath propagation*, Int. J. Remote Sensing, 19, 2283-2300, 1998.

**Gorbunov, M. E.**, *Radioholographic methods for processing radio occultation data in multipath regions*, Scientific Report 01-02, Danish Meteorological Institute, Copenhagen, 2001.

**Gorbunov, M. E.**, *Radioholographic analysis of Microlab-1 radio occultation data in the lower troposphere*, J. Geophys. Res. 107(D12), 10.1029/2001JD000889, 2002a.

**Gorbunov, M. E.**, 2002, *Canonical transform method for processing GPS radio occultation data in lower troposphere*, Radio Science, 37(5), 10.1029/2000RS002592, 2002b.

**Gorbunov, M. E.**, Benzon, H.- H., Jensen, A. S., Lohmann, M., Nielsen, A. S., *Comparative analysis of radio occultation processing approaches based on Fourier integral operators*. Submitted to Radio Sci. 2003.

**Gorbunov, M. E.**, *Analysis of wave fields by Fourier integral Operators and their application for radio occultations: additional notes*. Unpublished 2003.

---

**Harris, F.J.**, *On the use of windows for harmonic analysis with the discrete Fourier transform*, Proceedings of the IEEE, 66, p. 51-83, 1978.

**Hinson, D. P.**, F. M. Flasar, A. J. K. P. J. Schinder, J. D. Twicken, and R. G. Herrera, *Jupiter's Ionsphere: Results from the first Galileo radio occultation experiment*, Geophys., Res. Lett., 24(17), 2107-2110, 1997.

**Hinson, D. P.**, J. D. Twicken, and E. T. Karayel, *Jupiter's Ionsphere: New Results from the first Voyager2 radio occultation measurements*, J. Geophys. Res., 103(A5), 9505-9520, 1998.

**Hocke, K. A.**, A. G. Pavelyev, O. I. Yakovlev, L. Barthes, and N. Jakowski, *Radio occultation data analysis by the radioholographic method*, J. Atmos. Sol.Terr. Phys., 61(15) 1169-117, 1999.

**Høeg, P.**, Kirchengast, G., *ACE+: Atmosphere and Climate Explorer*, proposal to ESA in response to the second call for proposals for Earth Explorer Opportunity Missions, 2002.

**International Telecommunication Union**, *Propagation in non-ionized media*, J. Comp. Phys., 41, 115-131, 1981.

**Jensen, A. S.**, Benzon H. H, Lohmann M., *A New High Resolution Method for Processing Radio Occultation Data*, Scientific Report 02-06, ISSN no. 0905-3263, ISBN no. 87-7478-458-7, Danish Meteorological Institute, Copenhagen 2002.

**Jensen, A. S.**, Lohmann, M., Benzon, H.-H., Nielsen, A.S. *Full Spectrum Inversion of Radio Occultation Signals*, Radio Sci. Vol. 38, No. 3 10.1029/2002RS002763, 21 May, 2003a.

**Jensen, A. S.**, Lohmann, M., Benzon, H.-H., Nielsen, A.S. *Geometrical Optics Phase Matching of Radio Occultation Signals*, Radio Sci., under review, 2003b.

**Kursinski, E. R.**; Hajj, G.A.; Schofield, J.T.; Linfield, R. P.; Hardy, K. R. *Observing Earth's atmosphere with radio occultation measurements using the Global Positioning System*, JGR 102, p. 23429-23466, 1997.

**Kursinski, E. R.**, Leroy, S.S., and Herman, B, *The Radio Occultation Technique*, Terr. Atmos. Oceanic Sci. 11, 53-114, 2000.

**Kursinski, E. R.**, S. Syndergaard, D. Flittner, D. Feng, G. Hajj, B. Herman, D. Ward, and T. Yunck. *A microwave occultation observing system optimized to characterize atmospheric water, temperature and Geopotential via absorption*. Journal of Atmospheric and Oceanic Technology, 19(12), 1897 -1914, 2002.

**Leroy, S. S.** *The Diffraction Calculation (diffprop)*, unpublished 2001a.

**Leroy, S. S.**, *Active Microwave Limb-sounding for Tropospheric Water Vapor: Some Theoretical Considerations*, unpublished 2001b.

- 
- Liebe, H. j.**, MPM – *An atmospheric millimeter-wave propagation model*, int. J. Infrared Millimeter Waves, 10, 631-650, 1989.
- Lindal, G. F.**, J. R. Lyons, D. N. Sweetnam, V. R. Eshleman, D. P. Hinson, and G. L. Tyler, *The atmosphere of Uranus: Results of radio occultation measurements with Voyager 2*, J. Geophys. Res., 92(A13), 14,987-001, 1987.
- Lohmann, M. S.**, L. Olsen, H.-H. Benzon, A. S. Nielsen, A. S. Jensen, P. Høeg, *Water vapour profiling using LEO-LEO inter-satellite links*, Proceedings of the symposium "Atmospheric Remote Sensing using Satellite Navigation Systems", URSI
- Marouf, E.A.**, G. L. Tyler, and P.A. Rosen, *Profiling Saturn's rings by radio occultation*, Icarus, 68, 120-166, 1986.
- Mortensen, M.D.**, and P. Høeg, *Inversion of GPS occultation measurements using Fresnel diffraction theory*, Geophysical Research Letters, 25, 2441-2444, 1998a.
- Meincke, M. D.**, *Inversion methods for atmospheric profiling with GPS occultations*. Scientific Report 99-11, Danish Meteorological Institute, Copenhagen, 1999.
- Nielsen, A. S.**, M. S. Lohmann, P. Høeg, H.-H. Benzon, A. S. Jensen, T. Kuhn., C. Melsheimer, S. A. Buehler, P. Eriksson, L. Gradinarsky, C. Jimenez, G. Elgered, *Characterization of ACE+ LEO-LEO Radio Occultation Measurements*, ESTEC Contract NO. 16743/02/NL/FF. 2003.
- Pavelyev, A. G.**, *On the feasibility of radioholographic investigations of wave fields near the Earth's radio-shadow zone on the satellite-to-satellite path*, J. Commun Technol. Electron., 43(8), 875-879, 1998.
- Proakis, J. G.**, D. G. Manolakis, *Digital signal processing principles, algorithms, and applications*, 3<sup>rd</sup> edition, Prentice-Hall, Inc., 1996.
- Rocken, C.**, R.A. Anthes, M. Exner, D. Hunt, S. Sokolovskiy, R. Ware, M. Gorbunov, W. Schreiner, D. Feng, B. Herman, Y.H. Kuo and X. Zou, *Analysis and validation of GPS/MET data in the neutral atmosphere*, Journal of Geophysical Research, 102, 29,849-29,866, 1997.
- Sokolovskiy, S. V.**, *Modeling and inverting radio occultation signals in the moist troposphere*. Radio Sci., 36(3), 441-458, 2001.
- Sokolovskiy, S. V.**, *Inversion of radio occultation amplitude data*. Radio Sci., 35(1), 97-105, 2000.

---

## DANISH METEOROLOGICAL INSTITUTE

### Scientific Reports

Scientific reports from the Danish Meteorological institute cover a variety of geophysical fields, i.e., meteorology (including climatology), oceanography, subjects on air and sea pollution, geomagnetism, solar-terrestrial physics, and physics of the middle and upper atmosphere.

Reports in the series within the last five years:

No. 98-1

**Niels Woetman Nielsen, Bjarne Amstrup, Jess U. Jørgensen:**

HIRLAM 2.5 parallel tests at DMI: sensitivity to type of schemes for turbulence, moist processes and advection

No. 98-2

**Per Høeg, Georg Bergeton Larsen, Hans-Henrik Benzon, Stig Syndergaard, Mette Dahl**

**Mortensen:** The GPSOS project Algorithm functional design and analysis of ionosphere, stratosphere and troposphere observations

No. 98-3

**Mette Dahl Mortensen, Per Høeg:**

Satellite atmosphere profiling retrieval in a nonlinear troposphere Previously entitled: Limitations induced by Multipath

No. 98-4

**Mette Dahl Mortensen, Per Høeg:**

Resolution properties in atmospheric profiling with GPS

No. 98-5

**R.S. Gill and M. K. Rosengren**

Evaluation of the Radarsat imagery for the operational mapping of sea ice around Greenland in 1997

No. 98-6

**R.S. Gill, H.H. Valeur, P. Nielsen and K.Q. Hansen:**

Using ERS SAR images in the operational mapping of sea ice in the Greenland waters: final report for ESA-ESRIN's: pilot projekt no. PP2.PP2.DK2 and 2<sup>nd</sup> announcement of opportunity for the exploitation of ERS data projekt No. AO2..DK 102

No. 98-7

**Per Høeg et al.:** GPS Atmosphere profiling methods and error assessments

No. 98-8

**H. Svensmark, N. Woetmann Nielsen and A.M. Sempreviva:** Large scale soft and hard turbulent states of the atmosphere

No. 98-9

**Philippe Lopez, Egil Kaas and Annette Guldborg:** The full particle-in-cell advection scheme in spherical geometry

No. 98-10

**H. Svensmark:** Influence of cosmic rays on earth's climate

No. 98-11

**Peter Thejll and Henrik Svensmark:** Notes on the method of normalized multivariate regression

No. 98-12

**K. Lassen:** Extent of sea ice in the Greenland Sea 1877-1997: an extension of DMI Scientific Report 97-5

No. 98-13

**Niels Larsen, Alberto Adriani and Guido Donfrancesco:** Microphysical analysis of polar stratospheric clouds observed by lidar at McMurdo, Antarctica

No.98-14

---

**Mette Dahl Mortensen:** The back-propagation method for inversion of radio occultation data

No. 98-15

**Xiang-Yu Huang:** Variational analysis using spatial filters

No. 99-1

**Henrik Feddersen:** Project on prediction of climate variations on seasonal to interannual timescales (PROVOST) EU contract ENV4-CT95-0109: DMI contribution to the final report: Statistical analysis and post-processing of uncoupled PROVOST simulations

No. 99-2

**Wilhelm May:** A time-slice experiment with the ECHAM4 A-GCM at high resolution: the experimental design and the assessment of climate change as compared to a greenhouse gas experiment with ECHAM4/OPYC at low resolution

No. 99-3

**Niels Larsen et al.:** European stratospheric monitoring stations in the Arctic II: CEC Environment and Climate Programme Contract ENV4-CT95-0136. DMI Contributions to the project

No. 99-4

**Alexander Baklanov:** Parameterisation of the deposition processes and radioactive decay: a review and some preliminary results with the DERMA model

No. 99-5

**Mette Dahl Mortensen:** Non-linear high resolution inversion of radio occultation data

No. 99-6

**Stig Syndergaard:** Retrieval analysis and methodologies in atmospheric limb sounding using the GNSS radio occultation technique

No. 99-7

**Jun She, Jacob Woge Nielsen:** Operational wave forecasts over the Baltic and North Sea

No. 99-8

**Henrik Feddersen:** Monthly temperature forecasts for Denmark - statistical or dynamical?

No. 99-9

**P. Thejll, K. Lassen:** Solar forcing of the Northern hemisphere air temperature: new data

No. 99-10

**Torben Stockflet Jørgensen, Aksel Walløe Hansen:** Comment on "Variation of cosmic ray flux and global coverage - a missing link in solar-climate relationships" by Henrik Svensmark and Eigil Friis-Christensen

No. 99-11

**Mette Dahl Meincke:** Inversion methods for atmospheric profiling with GPS occultations

No. 99-12

**Hans-Henrik Benzon; Laust Olsen; Per Høeg:** Simulations of current density measurements with a Faraday Current Meter and a magnetometer

No. 00-01

**Per Høeg; G. Leppelmeier:** ACE - Atmosphere Climate Experiment

No. 00-02

**Per Høeg:** FACE-IT: Field-Aligned Current Experiment in the Ionosphere and Thermosphere

No. 00-03

**Allan Gross:** Surface ozone and tropospheric chemistry with applications to regional air quality modeling. PhD thesis

No. 00-04

**Henrik Vedel:** Conversion of WGS84 geometric heights to NWP model HIRLAM geopotential heights

No. 00-05

**Jérôme Chenevez:** Advection experiments with DMI-Hirlam-Tracer

No. 00-06

**Niels Larsen:** Polar stratospheric clouds micro-physical and optical models

No. 00-07

---

**Alix Rasmussen:** "Uncertainty of meteorological parameters from DMI-HIRLAM"

No. 00-08

**A.L. Morozova:** Solar activity and Earth's weather. Effect of the forced atmospheric transparency changes on the troposphere temperature profile studied with atmospheric models

No. 00-09

**Niels Larsen, Bjørn M. Knudsen, Michael Gauss, Giovanni Pitari:** Effects from high-speed civil traffic aircraft emissions on polar stratospheric clouds

No. 00-10

**Søren Andersen:** Evaluation of SSM/I sea ice algorithms for use in the SAF on ocean and sea ice, July 2000

No. 00-11

**Claus Petersen, Niels Woetmann Nielsen:** Diagnosis of visibility in DMI-HIRLAM

No. 00-12

**Erik Buch:** A monograph on the physical oceanography of the Greenland waters

No. 00-13

**M. Steffensen:** Stability indices as Indicators of lightning and thunder

No. 00-14

**Bjarne Amstrup, Kristian S. Mogensen, Xiang-Yu Huang:** Use of GPS observations in an optimum interpolation based data assimilation system

No. 00-15

**Mads Hvid Nielsen:** Dynamisk beskrivelse og hydrografisk klassifikation af den jyske kyststrøm

No. 00-16

**Kristian S. Mogensen, Jess U. Jørgensen, Bjarne Amstrup, Xiaohua Yang and Xiang-Yu Huang:** Towards an operational

implementation of HIRLAM 3D-VAR at DMI

No. 00-17

**Sattler, Kai; Huang, Xiang-Yu:** Structure function characteristics for 2 meter temperature and relative humidity in different horizontal resolutions

No. 00-18

**Niels Larsen, Ib Steen Mikkelsen, Bjørn M. Knudsen m.fl.:** In-situ analysis of aerosols and gases in the polar stratosphere. A contribution to THESEO. Environment and climate research programme. Contract no. ENV4-CT97-0523. Final report

No. 00-19

**Amstrup, Bjarne:** EUCOS observing system experiments with the DMI HIRLAM optimum interpolation analysis and forecasting system

No. 01-01

**V.O. Papitashvili, L.I. Gromova, V.A. Popov and O. Rasmussen:** Northern polar cap magnetic activity index PCN: Effective area, universal time, seasonal, and solar cycle variations

No. 01-02

**M.E. Gorbunov:** Radiological methods for processing radio occultation data in multipath regions

No. 01-03

**Niels Woetmann Nielsen; Claus Petersen:** Calculation of wind gusts in DMI-HIRLAM

No. 01-04

**Vladimir Penenko; Alexander Baklanov:** Methods of sensitivity theory and inverse modeling for estimation of source parameter and risk/vulnerability areas

No. 01-05

**Sergej Zilitinkevich; Alexander Baklanov; Jutta Rost; Ann-Sofi Smedman, Vasilij Lykosov and Pierluigi Calanca:** Diagnostic and prognostic equations for the depth of the stably stratified Ekman boundary layer

No. 01-06

---

**Bjarne Amstrup:** Impact of ATOVS AMSU-A radiance data in the DMI-HIRLAM 3D-Var analysis and forecasting system

No. 01-07

**Sergej Zilitinkevich; Alexander Baklanov:** Calculation of the height of stable boundary layers in operational models

No. 01-08

**Vibeke Huess:** Sea level variations in the North Sea – from tide gauges, altimetry and modelling

No. 01-09

**Alexander Baklanov and Alexander Mahura:** Atmospheric transport pathways, vulnerability and possible accidental consequences from nuclear risk sites: methodology for probabilistic atmospheric studies

No. 02-01

**Bent Hansen Sass and Claus Petersen:** Short range atmospheric forecasts using a nudging procedure to combine analyses of cloud and precipitation with a numerical forecast model

No. 02-02

**Erik Buch:** Present oceanographic conditions in Greenland waters

No. 02-03

**Bjørn M. Knudsen, Signe B. Andersen and Allan Gross:** Contribution of the Danish Meteorological Institute to the final report of SAMMOA. CEC contract EVK2-1999-00315: Spring-to-autumn measurements and modelling of ozone and active species

No. 02-04

**Nicolai Kliem:** Numerical ocean and sea ice modelling: the area around Cape Farewell (Ph.D. thesis)

No. 02-05

**Niels Woetmann Nielsen:** The structure and dynamics of the atmospheric boundary layer

No. 02-06

**Arne Skov Jensen, Hans-Henrik Benzon and Martin S. Lohmann:** A new high resolution method for processing radio occultation data

No. 02-07

**Per Høeg and Gottfried Kirchengast:** ACE+: Atmosphere and Climate Explorer

No. 02-08

**Rashpal Gill:** SAR surface cover classification using distribution matching

No. 02-09

**Kai Sattler, Jun She, Bent Hansen Sass, Leif Laursen, Lars Landberg, Morten Nielsen og Henning S. Christensen:** Enhanced description of the wind climate in Denmark for determination of wind resources: final report for 1363/00-0020: Supported by the Danish Energy Authority

No. 02-10

**Michael E. Gorbunov and Kent B. Lauritsen:** Canonical transform methods for radio occultation data

No. 02-11

**Kent B. Lauritsen and Martin S. Lohmann:** Unfolding of radio occultation multipath behavior using phase models

No. 02-12

**Rashpal Gill:** SAR ice classification using fuzzy screening method

No. 02-13

**Kai Sattler:** Precipitation hindcasts of historical flood events

No. 02-14

**Tina Christensen:** Energetic electron precipitation studied by atmospheric x-rays

No. 02-15

**Alexander Mahura and Alexander Baklanov:** Probabilistic analysis of atmospheric transport patterns from nuclear risk sites in Euro-Arctic Region

No. 02-16

---

**A. Baklanov, A. Mahura, J.H. Sørensen, O. Rigina, R. Bergman:**  
Methodology for risk analysis based on atmospheric dispersion modelling from nuclear risk sites

**A. Mahura, A. Baklanov, J.H. Sørensen, F. Parker, F. Novikov K. Brown, K. Compton:**  
Probabilistic analysis of atmospheric transport and deposition patterns from nuclear risk sites in russian far east

No. 02-17